Nucleosynthesis at the termination point of the *s* process

U. Ratzel, C. Arlandini, and F. Käppeler*
Institut für Kernphysik, Forschungszentrum Karlsruhe, P.O. Box 3640, D-76021 Karlsruhe, Germany

A. Couture and M. Wiescher
Physics Department, University of Notre Dame, Notre Dame, Indiana 46556, USA

R. Reifarth
Los Alamos National Laboratory, Los Alamos, New Mexico 87545, USA

R. Gallino
Dipartimento di Fisica Generale, Università di Torino and Sezione INFN di Torino, Via P. Giuria 1, I-10125 Torino, Italy and Centre for Stellar and Planetary Astrophysics, School of Mathematical Sciences, Monash University, Melbourne 3800, Australia

A. Mengoni
CERN, CH-1211 Geneva 23, Switzerland

C. Travaglio
Max-Planck-Institut für Astrophysik, Postfach 1523, D-85740 Garching, Germany and Istituto Nazionale di Astrofisica (INAF), Osservatorio Astronomico di Torino, Strada Osservatorio 20, I-10025 Pino Torinese (To), Italy

(Received 6 October 2003; revised manuscript received 23 July 2004; published 10 December 2004)

Stellar cross sections of importance with respect to the termination of the *s*-process reaction chain have been determined for the two cases, ^{208}Pb$(n,\gamma)^{209}$Pb and ^{209}Bi$(n,\gamma)^{210}$Bi^{g}, yielding $kT=30$ keV values of $\langle\sigma v\rangle/v_T = 0.31\pm0.2$ mb and 2.54 ± 0.14 mb, respectively. The measurements were carried out by activation of Pb and Bi samples in a quasistellar neutron spectrum using gold as a cross section standard. With this technique the uncertainties reported in previous works could be considerably reduced. The measurements are complemented by a discussion of the recycling at the termination point of the *s*-process neutron capture chain in a $3M_{\odot}$ and $[\mathrm{Fe/H}]=-1.3$ asymptotic giant branch star. At this metallicity, AGB stars give rise to the maximum production of *s*-process lead. The sensitivity of the isotopic lead abundances is discussed with respect to the remaining cross section uncertainties. The information obtained in this work is also of relevance for an assessment of the α activity due to a buildup of ^{210}Po in Pb/Bi cooled fast reactor systems.

DOI: 10.1103/PhysRevC.70.065803 PACS number(s): 25.40.Lw, 26.20.+f, 27.80.+w, 97.10.Cv

I. THE TERMINATION POINT OF THE *s* PROCESS: A CHALLENGE FOR EXPERIMENTS AND MODELS

The origin of the isotopes in the atomic mass range $A=204-210$ can be attributed to the main neutron capture processes, the *s* and *r* processes. Quantitative analyses are complicated because both processes exhibit specific peculiarities in this region. Further neutron captures on ^{209}Bi, the last stable *s*-process nucleus, into the region of α-unstable isotopes result in a certain probability for recycling via α decays and a corresponding accumulation of *s*-process material beyond ^{206}Pb. The *s* component is also affected by a branching at ^{204}Tl, which causes the reaction flow to partially bypass the *s*-only isotope ^{204}Pb. The *r* process contributes a strong radiogenic component to the ^{206}Pb and ^{207}Pb abundances by decays from the transbismuth region, in addition to the primary *r*-process yields in the $A=206/207$ chains.

The decomposition of this complex abundance pattern by the classical *s* process [1–3] turned out to be difficult because these analyses failed to account for the abundances of ^{208}Pb and ^{209}Bi. For example, the contributions from the classical *s* process and the *r* component obtained by assuming a smooth *r*-abundance distribution in this mass range provided less than half of the ^{208}Pb observed. For this reason, a *strong* component of the *s* process responsible for the production of these heavy isotopes was postulated [2] to produce the missing ^{208}Pb and ^{209}Bi. However, a plausible astrophysical site for this additional *s* process could not be identified.

A natural explanation was found when detailed stellar *s*-process models were used to investigate galactic chemical evolution [4,5]. In these studies, the strong component was found to be associated with the *s* process operating in early generation, low-metallicity, low-mass, thermally pulsing asymptotic giant branch (AGB) stars. In light of this improved picture, it becomes increasingly important to establish reliable nuclear physics data for a quantitative discussion of the abundances at the end of the *s*-process path.

*Electronic address: franz.kaeppeler@ik.fzk.de

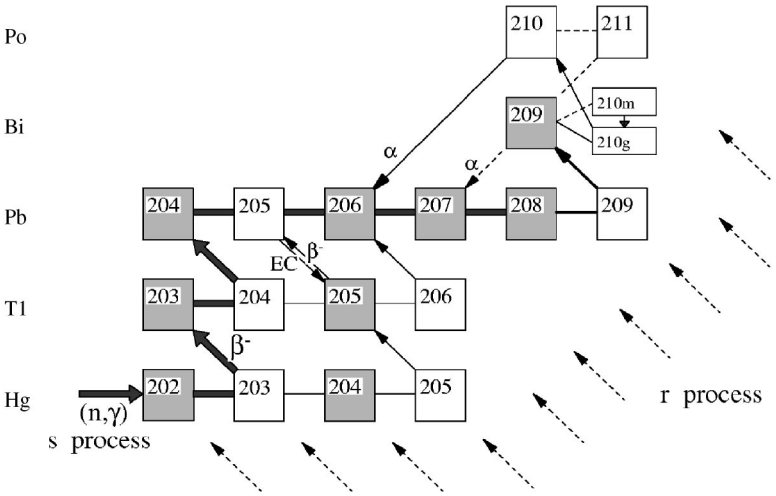

FIG. 1. The reaction network at the end of the *s*-process path. Stable isotopes are indicated with shaded boxes. Note, that the recycling effect via the α-unstable polonium isotopes is weak. Most of the reaction flow is trapped at ^{208}Pb and ^{209}Bi because of the small (n,γ) cross sections of these neutron magic nuclei. Because the isomeric state in ^{210}Bi is quickly depopulated to the short-lived ground state by the hot photon bath at *s*-process temperatures, its α-decay and neutron capture contributions are negligible.

Figure 1 illustrates the *s*-process reaction network between Tl and Po. When the neutron capture chain reaches ^{209}Bi, the next captures feed the α-unstable trans-bismuth isotopes, which terminate the production of heavier nuclei and start recycling the *s*-process flow to ^{206}Pb and ^{207}Pb. These contributions, which are determined by the role of the isomer ^{210}Bi^m and a possible branching at ^{210}Po, are important for unraveling the radiogenic contributions to the isotopic Pb abundances from the Th and U decays.

The Th/U cosmochronometer has attracted great interest due to the recent determination of accurate actinide abundances in old, extremely metal-poor stars [6,7]. These observations provide a chronometer *independent* of models for galactic evolution, thus avoiding one of the primary weaknesses of previous attempts to interpret the Th/U abundance ratios as a cosmic clock [8]. Representing the final products of the Th/U α-decay chains, the isotopic abundances of Pb provide an additional constraint to consolidate the reliability of this chronometer. In particular, the *s*-process production needs to be determined self-consistently in order to separate the remaining radiogenic contribution and the corresponding *r*-process yields. For this to be done, the cross sections of the Pb isotopes, and especially that of ^{207}Pb—an *s*-only isotope, shielded from the *r* process by its mercury isobar—must be accurately known because they are required to define the *s*-process abundances.

A third motivation for improving the Pb cross sections is the analysis of the *s*-process branching at ^{204}Tl, which determines the abundance of ^{204}Pb. This branching, which is not affected by the recycling at the termination point, is of interest because the half-life of ^{204}Tl exhibits a pronounced temperature dependence [9]. Therefore, it serves not only as a calibration of the strength of the *s* process at these heavy isotopes, but also as an *s*-process thermometer.

At present, the status of the respective nuclear data in the $A=204-210$ region is unsatisfactory. For the unstable branch point isotopes ^{204}Tl and ^{205}Pb, only theoretical cross sections are known. The available experimental cross sections for ^{204}Pb and for ^{206}Pb exhibit significant discrepancies indicating that systematic uncertainties exist in the data obtained with the time-of-flight (TOF) technique that were not recognized in the respective experiments. More recent data were reported for ^{207}Pb, ^{208}Pb, and ^{209}Bi [10,11] with uncertainties between 9% and 14%, yet not sufficient to characterize the *s* abundances with the required accuracy of $\approx$5%, which is mandatory for reliable analyses. Moreover, TOF measurements are sensitive only to capture resonances, not to the direct capture component of the cross section. Because the direct capture contribution is fairly large for neutron magic nuclei, the activation technique was used to obtain experimental information on this part as well. The technique outlined in this paper has recently been used to extend the activation measurements to higher energies [12].

We present activation measurements of the (n,γ) cross-sections for ^{208}Pb and ^{209}Bi$(n,\gamma)^{210}$Bi^g. In Sec. II we discuss the method of the measurements and the results. In Sec. III we incorporate these rates in the *s* process and discuss its implications as well as the consequences of the remaining cross section uncertainties. Section IV will summarize these results with emphasis on further nuclear data needs and the potential for meeting them.

II. CROSS SECTION MEASUREMENTS

These measurements take advantage of the activation technique [13], which is particularly suited for determining the very small cross sections at magic neutron numbers where traditional time-of-flight experiments are complicated by the enormous background from the dominant elastic-scattering channel. This background and the related large corrections are completely avoided in activation measurements, which, therefore, represent an important complementary approach. Though this technique is limited to special *s*-process conditions, it yields accurate data to be used either directly in *s*-process calculations or to test the reliability of existing time-of-flight data.

The measurements presented here differ from typical activations; the induced activities cannot be detected via γ-spectroscopy with Ge detectors. Because the respective product nuclei ^{209}Pb and ^{210}Bi^g decay directly or predominantly to the ground state of their respective daughters (Fig. 2), the β-decay electrons have to be detected instead, which requires the use of thin samples as well as a careful check for parasitic activation of possible sample impurities. In order to

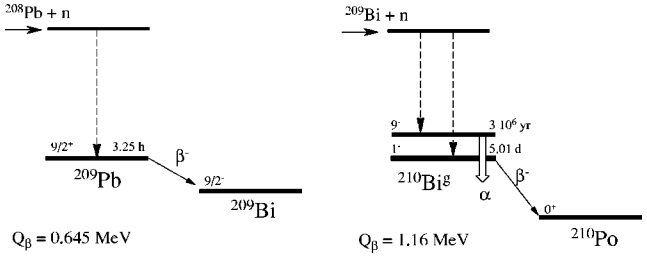

FIG. 2. Decay schemes of ^{209}Pb and ^{210}Bi^{g} illustrating the features of the present activations.

achieve reliable data, the corresponding loss in experimental sensitivity must be compensated by detectors with very high efficiency.

A. Sample preparation

The samples were prepared in two ways. All of the Bi samples as well as one of the Pb samples were evaporated onto thin ($10-25$ μg/cm^2) FORMVAR foils stretched over thin aluminum rings with an inner diameter of 33 mm. The thicknesses of the FORMVAR foils were determined prior to the evaporation by weighing them. For the Bi targets, a high-purity Bi metal was used in the evaporator. A 10 mm mask together with a 25 cm separation between the boat and the FORMVAR foil ensured that the sample was homogeneous. Due to the relatively low melting point of Bi (217.3 °C), there was no difficulty in producing Bi layers between 1 and 5 mg/cm^2. The evaporated Pb target was made from a highly enriched sample of ^{208}Pb. As such, a distance of only 5 cm was used between the boat and the sample. An initial estimate of the mass of the samples was made by weighing the FORMVAR foils (with the Al ring) before and after the evaporation. The value used for the mass of the samples was determined by removing the target from the holder ring and weighing it after the experiment was completed. Targets Bi1, Bi2, Bi3, and Pb3 were prepared in this way.

The other Pb targets were prepared by punching 10-mm-diam foils of very pure, natural Pb. The Pb foils were weighed and then sandwiched between thin FORMVAR foils. Lead targets Pb1, Pb2, and Pb4 were produced in this manner.

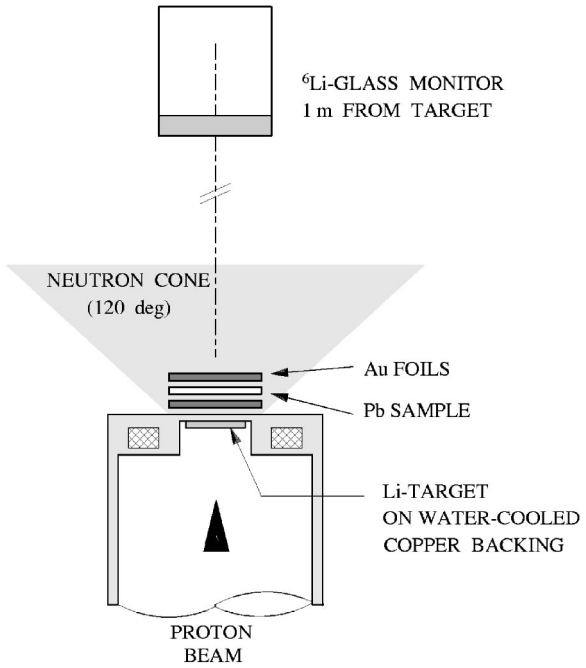

FIG. 3. Sketch of the activation setup at the Van de Graaff accelerator.

Gold foils were used to monitor the neutron flux during the experiment. For all of the Bi samples, a thin (0.03 mm) gold foil was placed on top of the FORMVAR foil. Because a beta spectrum was needed for the Pb targets, an evaporated layer of gold was used to monitor the neutron flux for all the Pb targets. In this way, systematic uncertainties in counting the induced activities were considerably reduced. Table I contains all of the relevant information concerning the targets used in this experiment.

B. Activations

The neutron exposure was produced using the 3.7 MV Van de Graaff accelerator (Fig. 3) at Forschungszentrum Karlsruhe by exploiting the ^{7}Li$(p,n)^{7}$Be reaction at E_p = 1921 keV. This results in a quasi-Maxwellian energy dis-

TABLE I. Sample characteristics.

Sample	Production technique	Isotopic composition	Area density (mg/cm^2)
		^{208}Pb samples	
Pb1	punched foil	natural (52.4±0.1%)	3.38±0.7%
Pb2	punched foil	natural (52.4±0.1%)	2.13±1.0%
Pb3	evaporated	enriched (98.7±0.3%)	1.06±2.1%
Pb4	punched foil	natural (52.4±0.1%)	4.93±0.5%
		^{209}Bi samples	
Bi1	evaporated	natural (100%)	3.65±0.7%
Bi2	evaporated	natural (100%)	5.50±0.5%
Bi3	evaporated	natural (100%)	1.32±1.9%

TABLE II. Relevant parameters of the various activations.

Run	Sample	Duration (h)	Average flux (10^8 s^{-1})	Counting time (h)	Counts (threshold in keV)	Signal/Bckgd
			^{208}Pb samples			
1	Pb1	6.7	7.8	6.0	7410 (25)	0.35
2	Pb2	5.5	10	6.0	5020 (35)	0.63
3	Pb3	8.5	4.8	5.5	3020 (25)	0.34
4	Pb4	6.3	6.6	6.0	9940 (15)	0.93
			^{209}Bi samples			
5	Bi1	35	3.9	20	110930 (15)	3.3
6	Bi2	35	6.2	20	233260 (15)	6.8
7	Bi3	44	6.9	15	51125 (15)	2.0

tribution of neutrons with $kT=25$ keV. For the details of this technique, the reader is referred to Ref. [14].

For all activations, the beam diameter was slightly larger than the target size, so only the mass of the target was relevant. Because the gold foils and samples were in direct contact, the correction due to the difference in the solid angle between the two was small. This effect was measured, and it was found that a separation by 0.1 mm would cause a 1.5% difference in neutron flux. Nonetheless, an uncertainty of 2.5% was assumed for this effect in case the sample could have slightly separated from the gold foil during the activation.

During all the activation cycles, a ^{6}Li glass scintillator was used to monitor the neutron flux in 1–2 min intervals. This allows one to calculate the correction factor f_b, which numerically corrects for the decay of the induced activity that occurs already during irradiation (for details see Ref. [13]). The features of the various activations are summarized in Table II.

C. Activity counting

A 4π electron spectrometer consisting of two Si(Li) detectors in close geometry was used to measure the β spectra (Fig. 4). The entrance windows of the Si(Li) detectors, which had a sensitive area 16 mm diam, consisted of an evaporated gold layer of 20 μg/cm^2 and were held at ground potential. The resolution was 0.4% and 0.3% at 0.5 and 1.0 MeV electron energy, respectively. The detectors were separated by less than 1 mm, resulting in an effective solid angle of 93.5% of 4π. This required that the positions of the detectors and of the sample could be reliably reproduced. For the sample this was achieved by means of a conical guide. The Si(Li) detectors were mounted on calibrated micrometers.

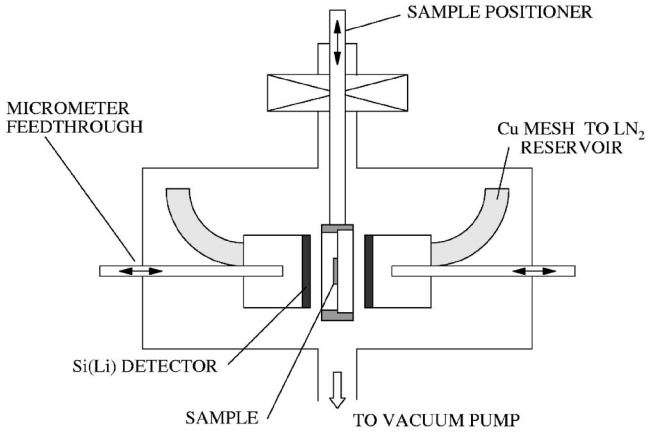

FIG. 4. Schematic setup of the 4π electron spectrometer.

During the activity measurements the spectrometer was evacuated to 6×10^{-6} Pa and a sluice allowed the samples to be changed in ~2 min without breaking the vacuum. The detectors were cooled with liquid nitrogen to a temperature of 110 K. In the relevant electron energy interval between 15 and 1000 keV, the general room background could be reduced to a rate of 0.49 s^{-1} by a lead shield. The setup was insensitive to electron backscattering from the detectors because the signals of both detectors were summed together. Figure 5 shows examples of the electron spectra measured with activated Pb and Bi samples.

D. Efficiency of the electron spectrometer

The efficiency of the spectrometer was determined by comparing the β and γ activities of activated gold foils. The respective γ activity was measured with a high-purity Ge detector. The efficiency of the Ge detector ϵ_γ was defined to ±1.6% using a set of calibrated sources. The β efficiencies were then obtained by the expression

$$\epsilon_\beta = \epsilon_\gamma \frac{(1-e^{-\lambda t_\gamma})}{e^{-\lambda t_w}(1-e^{-\lambda t_\beta})}\frac{N_\beta}{N_\gamma}K \qquad (1)$$

with the various terms denoting the efficiency of the Ge detector ϵ_γ, the counting time with the Ge detector t_γ, the counting time with the β spectrometer t_β, the corresponding waiting time between irradiation and counting t_w, the decay rate of ^{198}Au λ, and the number of observed events N_β and N_γ.

The correction factor K represents the product of the following five small contributions listed in Table III.

(i) Additional free electrons are produced as conversion electrons (k_1) and by Compton scattering of the 411.8 keV γ-rays (k_2). The latter contribution was measured using the 570 keV line from a calibrated ^{207}Bi source.

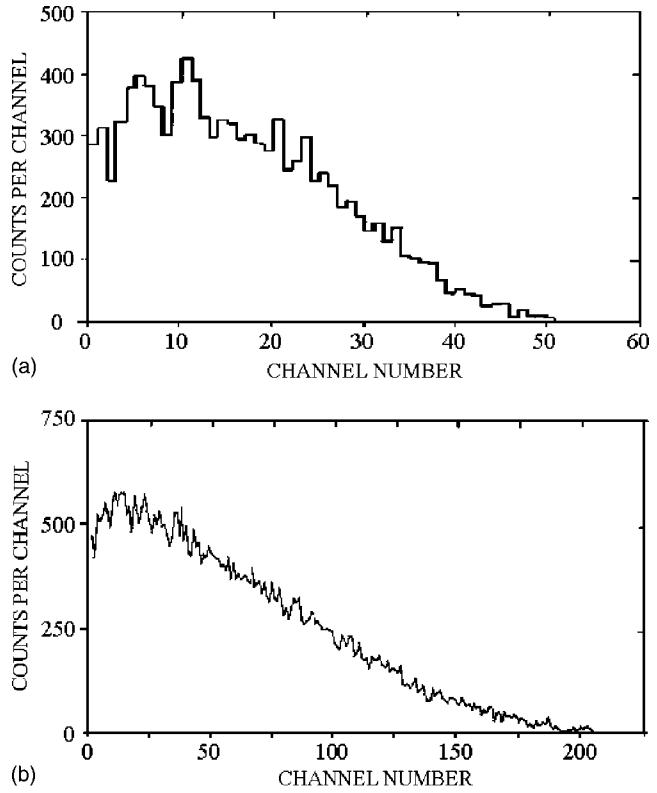

FIG. 5. The β^- spectra taken with samples Pb4 (top) and Bi3 (bottom).

(ii) Electrons are lost due to self-absorption in the 1.1 mg/cm^2 gold foils. This correction (k_3) was derived from theoretical estimates coupled with experimental data from the decay of ^{210}Bi^g, a decay with similar endpoint energy.

(iii) Because of the 15 keV threshold of the Si β-spectrometer, a correction (k_4) was necessary to extrapolate the electron spectra to zero energy.

(iv) Because ^{198}Au can decay to other states in ^{198}Hg besides the level at 411.8 keV while still emitting an electron, the branching ratio of this decay is to be considered (k_5).

The resulting detection efficiency of the 4π Si(Li) spectrometer was found to be $\epsilon_\beta = 0.935 \pm 0.016$.

E. Data analysis and results

Following the irradiations at the accelerator, the induced gold activities were measured via the 411.8 keV γ line, which could be detected with excellent statistics. The electron spectra showed signal-background ratios between 0.3 and 0.9 for the Pb samples and between 2 and 7 for the Bi samples.

TABLE III. Individual correction factors for the determination of ε_β.

Origin	Correction factor k_i
Conversion electrons	$k_1 = 0.995 \pm 0.001$
Compton electrons	$k_2 = 0.994 \pm 0.003$
Electron self-absorption	$k_3 = 1.015 \pm 0.008$
Spectrum extrapolation	$k_4 = 1.025 \pm 0.010$
Intensity of 411.8 keV Au decay line	$k_5 = 0.955 \pm 0.001$

The spectra were stored on disk in regular time intervals in order to check the decay curve for possible contributions from unexpected sample impurities. For ^{209}Pb, the half-life of $t_{1/2} = 3.2$ h could be perfectly reproduced, excluding such a correction at any significant level. The corresponding check for the half-life of the Bi samples confirmed that also in this case the effect of possible impurities was negligible (Fig. 6).

From the data collected in the various activations, (n, γ) cross sections were evaluated by the expression

$$\sigma_i = \sigma_{\mathrm{Au}} \frac{N_i}{N_{\mathrm{Au}}} \frac{m_{\mathrm{Au}}}{m_i} \frac{A_i}{A_{\mathrm{Au}}} \frac{f_{b,\mathrm{Au}}}{f_{b,i}} \frac{\epsilon_\gamma}{\epsilon_\beta} \frac{(1 - e^{-\lambda_{\mathrm{Au}} t_c}) e^{-\lambda_{\mathrm{Au}} t_w}}{(1 - e^{-\lambda_i t_c}) e^{-\lambda_i t_w}}, \quad (2)$$

where σ_{Au} is the gold cross section for the experimental, quasistellar spectrum corresponding to a thermal energy of $kT = 25$ keV, and N_{Au} and N_i are the number of events in the Au γ spectra and in the Pb/Bi electron spectra, respectively. Counting and waiting times are denoted by t_c and t_w, m are the sample masses, A the atomic weights, ϵ the detection efficiencies, and f_b the correction factors accounting for the decay during the activation. The resulting cross sections are listed in Table IV.

When plotted versus sample thickness, these data exhibit a nonnegligible trend indicating that the calculated correction for electron self-absorption in the sample was slightly underestimated. Accordingly, extrapolation to zero thickness yields the effective cross sections for the quasistellar neutron spectrum

$$\langle \sigma \rangle \left(^{208}\mathrm{Pb} \right) = 0.30 \pm 0.02 \text{ mb},$$

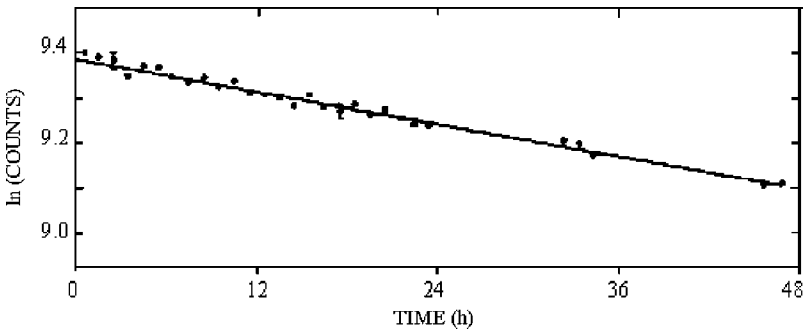

FIG. 6. The ^{210}Bi activity vs time fits perfectly to the well-known half-life, excluding significant background from activation of unexpected sample impurities.

TABLE IV. Experimental (n,γ) cross sections.

Run	Sample	Cross section (mb)
	^{208}Pb samples	
1	Pb1	0.265±0.015
2	Pb2	0.292±0.016
3	Pb3	0.292±0.015
4	Pb4	0.269±0.012
	^{209}Bi samples	
5	Bi1	2.46±0.10
6	Bi2	2.27±0.10
7	Bi3	2.45±0.10

$$\langle \sigma_p \rangle \left(^{209}\mathrm{Bi}\right) = 2.54 \pm 0.15 \text{ mb},$$

where the latter represents the partial cross section to the ground state of ^{210}Bi.

A final correction to these results is required because the experimental neutron spectrum is a good but not perfect simulation of a thermal distribution. In particular, the cutoff at 106 keV implies that the contributions from higher energies are not included. Such contributions come from two components, direct capture (DC) and single resonances. While the DC part is small at higher energies, resonance data from TOF measurements are found to imply an increase in the ^{208}Pb cross section by 2.7±0.6%. Hence, the final result for 25 keV thermal energy is $\langle\sigma\rangle_{25\ keV}$ (^{208}Pb) =0.31±0.02 mb. A similar correction for the partial ^{209}Bi cross section would require more detailed data than are presently available (see below).

The result for ^{208}Pb is in very good agreement with the time-of-flight measurement of Ref. [11], where a 25 keV cross section of 0.32±0.03 mb was reported. This agreement confirms that the corrections for scattered neutrons were properly treated in this case. Excellent agreement has also been found in the activation measurements reported by Beer *et al.* [12], which were extended to higher energies.

The partial stellar ^{209}Bi cross section feeding ^{210}Bi^g can be compared with a recent measurement at 40 keV [15]. If a $1/v$ shape of the cross section is assumed, the reported value of 2.08±0.23 mb is in very good agreement with the present result. The total reaction cross section has been determined in time-of-flight experiments. In a first attempt [16], data obtained in a limited energy range were used to renormalize previous cross sections, which obviously suffered from underestimated corrections for scattered neutrons. The resulting 25 keV average was found to be 1.8 mb, less than the partial cross section obtained in this work. A second high-resolution measurement [10] was performed with the same setup that was used for the ^{208}Pb experiment [11], where the corrections for scattered neutrons were better understood. The 25 keV average reported for the total (n,γ) cross section of 2.85±0.45 mb differs very little from the partial cross section to the ground state, in striking contrast to the situation for thermal neutrons, where the feeding probability of the ground state was only 72% [17] or even less [18].

This might result from the fact that a large fraction of the capture strength is to be attributed to narrow *p*-wave resonances. In fact, ^{210}Bi is in the mass region where the $l=1$ γ-ray strength function is at a maximum [19]. Consequently, if some of the narrow *p*-wave resonances are missed in differential measurements, part of the strength is lost. This situation does not apply to activation measurements. In the present case, because of the wide neutron energy range covered, the strength of all partial waves is included automatically.

This aspect is of relevance for the activity inventory in future advanced hybrid reactors, which will presumably be cooled with liquid Pb/Bi eutectic. As shown in Fig. 1, neutron captures on ^{209}Bi feed either the short-lived ground state and ultimately the α-emitter ^{210}Po with a half-life of 138 d, or the long-lived isomer ^{210}Bi^m, which is α-unstable with a half-life of 3×10^6 yr. Accordingly, the neutron capture cross section of ^{210}Bi determines the short-term as well as the long-term hazards in Pb/Bi cooled fast reactor systems.

F. Discussion of uncertainties

The efficiency of the Si(Li) detection system was measured with ^{204}Tl (E_0=763.5 keV) and ^{89}Sr (E_0=1.47 MeV) point sources. The related uncertainty was essentially determined by the activity of the calibration source (±1.5%) and by the correction for an extended source. Minor contributions to the final uncertainty of ±1.6% were due to the detector positions as well as to the corrections k_i discussed before.

Because an electronic threshold between 15 and 35 keV was needed in analyzing the electron spectra, an additional correction for the extrapolation to zero energy must be included. In the case of Pb, the uncertainty in the extrapolation was 2.0%, whereas for Bi it reduced to only 1.0% due to a higher end-point energy.

The uncertainty of the neutron flux was governed by uncertainties in positioning of the samples during the irradiations. In particular, any slight deformation of the FORMVAR foil could have affected the relative position with respect to the Au reference sample. This effect was studied experimentally with the evaporated gold samples. Based on these results a 2.5% uncertainty was attributed to the uncertainty in the sample position.

Another correction had to be made for the fact that the neutron spectrum was not a true Maxwell-Boltzmann distribution, mostly due to the cutoff at 106 keV. This gives rise to uncertainties when the cross section shape of the material being measured is not the same as that of the ^{197}Au standard. The correction for this difference adds an 0.6% uncertainty to the 1.5% uncertainty attributed to the ^{197}Au cross section itself [14].

The final corrections for electron self-absorption in the sample, which were obtained from the linear decrease of the cross section with sample thickness are listed in Table V.

III. IMPLICATIONS OF REACTION RATES FOR *s* ABUNDANCES IN THE Pb—Bi region

In this section, the *s*-process production of the lead and bismuth isotopes will be discussed on the basis of the present

TABLE V. Uncertainties (in %) of the individual activations. For several of the samples, no uncertainty is listed for the γ-detection efficiency because, in these cases, the activity of the gold foils was measured with the β spectrometer. Since the activations for the ^{209}Bi samples were much less than one day, the f_b factor can be neglected.

	^{208}Pb$(n,\gamma)^{209}$Pb				^{209}Bi$(n,\gamma)^{210}$Bi^g		
Source of uncertainty	Pb1	Pb2	Pb3	Pb4	Bi1	Bi2	Bi3
Sample mass	0.7	1.0	2.1	0.5	0.7	0.5	1.9
^{197}Au mass	0.2	0.2	0.2	0.2	0.2	0.2	0.2
^{197}Au cross section	1.5	1.5	1.5	1.5	1.5	1.5	1.5
γ-detection efficiency	1.6	1.6					
β-detection efficiency	2.5	2.5	1.6	1.6	1.6	1.6	1.6
E_β=0 extrapolation	2.0	2.0	2.0	2.0	1.0	1.0	1.0
Neutron flux	2.5	2.5	2.5	2.5	2.5	2.5	2.5
Decay during irradiation, f_b	0.5	0.5	0.5	0.5			
Isotopic enrichment	0.1	0.1	0.3	0.1			
Counting statistics	2.8	2.7	2.5	1.8	0.4	0.3	0.5
Background subtraction	1.0	1.0	1.0	1.0	2.0	2.0	2.0
Total uncertainty	5.6	5.6	5.2	4.5	4.1	4.1	4.5

results and the previously available cross section data. Starting from a present best set of input data, this discussion aims at assessing the effect of the remaining nuclear physics uncertainties on the specific astrophysical problems related to this particular mass region.

A. Stellar (n,γ) rates

The stellar cross sections in the mass region from ^{203}Tl to ^{210}Po, which are of direct relevance for this study, are listed in Table VI for a range of thermal energies. In this table the present results are complemented by data from the compilation of Ref. [20]. As far as the respective uncertainties are concerned, one finds that the 5% accuracy commonly required for reliable *s*-process abundance predictions, which had been met only for ^{206}Pb [21,22], have also been reached by the present results for ^{208}Pb and ^{209}Bi. Further efforts, preferentially based on advanced techniques and/or on different facilities, are, therefore, necessary to improve or to confirm previous TOF results in this mass region, where the (n,γ) cross sections are strongly influenced by nuclear struc-

TABLE VI. Stellar cross sections in the Tl to Po region (data from this work and from Ref. [20]). All values are in mb.

	Thermal energy (keV)								
Reaction	5	10	15	20	25	30	40	50	Comment
^{203}Tl$(n,\gamma)^{204}$Tl	330	307	214	167	140	124±8	93	76	expt
^{204}Tl$(n,\gamma)^{205}$Tl	874	412	317	269	238	215±38	183	161	calc
^{205}Tl$(n,\gamma)^{206}$Tl	102	89	74	65	58	54±4	46	40	expt
^{204}Pb$(n,\gamma)^{205}$Pb	168	139	118	105	96	90±6	80	73	expt
^{205}Pb$(n,\gamma)^{206}$Pb	604	268	197	162	140	125±22	104	91	calc
^{206}Pb$(n,\gamma)^{207}$Pb	25.5	23.4	21.0	17.3	16.2	15.8±0.8	15.1	14.3	expt
^{207}Pb$(n,\gamma)^{208}$Pb	13.9	12.3	12.3	11.6	10.7	9.7±1.3	8.1	6.9	expt
^{208}Pb$(n,\gamma)^{209}$Pb	0.06	0.12	0.20	0.27	0.32	0.36±0.04	0.39	0.41	expt
					0.31±0.02				this work
^{209}Bi$(n,\gamma)^{210}$Bi^g					2.54±0.14				this work
^{209}Bi$(n,\gamma)^{210}$Bi	11.3	6.1	4.3	3.4	2.9	2.7±0.5	2.5	2.3	expt
^{210}Bi$(n,\gamma)^{211}$Bi	18	10	8	7	7	6	5	5	calc
^{210}Po$(n,\gamma)^{211}$Po						3.3±3			calc

ture effects due to the proximity of closed neutron and proton shells.

In this context it is worth noting that the cross sections of the two unstable branch point isotopes, ^{204}Tl and ^{205}Pb, could be studied experimentally, provided that suitable samples be made available. This would be an important improvement compared to the procedure adopted in Ref. [20], where theoretically calculated Hauser-Feshbach rates are normalized to the experimental values of neighboring isotopes.

B. *s*-process contributions to Pb and Bi

As recalled in Sec. I, sufficient production of the heaviest isotopes at the end of the *s*-process path represented a major difficulty in the classical *s*-process model. The persistent underproduction of ^{208}Pb and ^{209}Bi by about a factor of two led to postulating a *strong* component tailored to account for the missing abundances. However, this strong component could not be linked to any plausible astrophysical site. The solution to this problem was not related to a separate *s* process, but appeared naturally from the standard *s*-process operating in low-metallicity, low-mass, thermally pulsing AGB stars [5,23].

The resulting *s*-process abundances are yet not accurate enough for quantitative analyses related to the branchings at ^{204}Tl and ^{205}Pb or to the U/Th cosmochronometer [24]. How much of this problem relates to the remaining cross uncertainties will be discussed in Sec. III C.

C. Sensitivity studies in the Pb/Bi region

The *s*-process abundances of the Pb and Bi isotopes exhibit a strong dependence on metallicity with a maximum production efficiency around $[\mathrm{Fe/H}]\approx -1$ (see Figs. 1 and 2 of Ref. [5]). The spectroscopic notation is defined as the logarithmic abundance ratio Fe/H relative to the solar value, $[\mathrm{Fe/H}]=\log(\mathrm{Fe/H})-\log(\mathrm{Fe/H})_{\odot}$. For example, the production factors of ^{208}Pb during He shell burning in low- and intermediate-mass AGB stars exceed the respective values for solar metallicity stars by two orders of magnitude. This enhanced efficiency is clearly reflected in the Pb abundances observed in some *s*-enriched metal-poor stars and must be considered in constraining galactic chemical evolution [25].

Therefore, a low-metallicity model star with $3M_{\odot}$ and $[\mathrm{Fe/H}]=-1.3$ was chosen to investigate how the final *s* abundances in the Pb/Bi region are affected by the presently remaining cross section uncertainties. This study was carried out by successive variation of the cross sections of all isotopes affecting the Pb abundances, including that of the branch point isotope ^{204}Tl.

This analysis is illustrated in Fig. 7 at the example of the standard case based on the cross sections listed in Table VI. The figure shows the *s*-process production factors for the Tl-Pb-Bi isotopes during the 25th thermal pulse in our $3M_{\odot}$, $[\mathrm{Fe/H}]=-1.3$ model star. All values are normalized to the final ^{204}Pb abundance. Isotopes, which are not part of the branching at ^{204}Tl, exhibit only small abundance variations throughout the entire thermal instability, whereas strong variations are observed for isotopes with $A=204$ and 205,

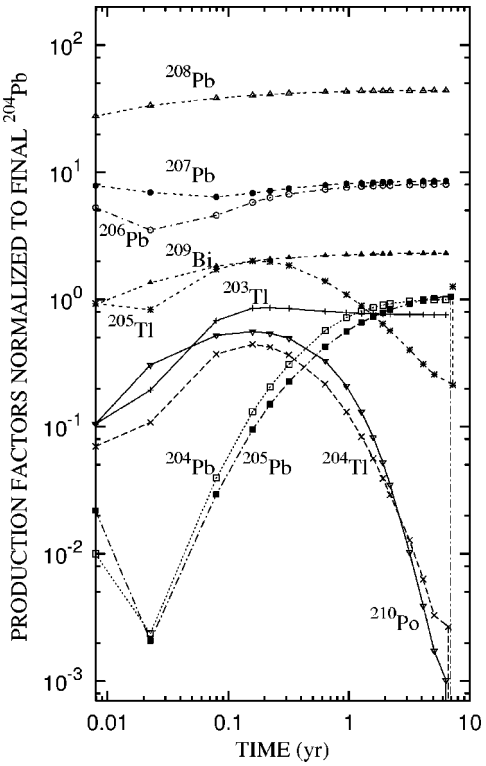

FIG. 7. Production factors for the Tl-Pb-Bi isotopes during the 25th thermal pulse in a $3M_{\odot}$ star with $[\mathrm{Fe/H}]=-1.3$. The data are normalized to the final ^{204}Pb abundance.

reflecting the pronounced changes of temperature and neutron density during the He-shell flash [23].

A good example in this respect is the *s*-only isotope ^{204}Pb. Between He shell flashes, the production of ^{204}Pb is marginal. In this phase, when the major ^{13}C neutron source operates at temperatures around 10^8 K, the half-life of ^{204}Tl is determined by the ground state decay ($t_{1/2}=3.26$ yr) so that neutron capture to ^{204}Tl dominates over β decay. During the comparably brief He shell flash episode shown in Fig. 7, temperatures of $T\approx 3\times 10^8$ K are reached. Under these conditions, the ^{204}Tl decay rate is enhanced by more than two orders of magnitude [9], resulting in a strong feeding of ^{204}Pb.

In the sensitivity analysis for the $M=3M_{\odot}$, $[\mathrm{Fe/H}]=-1.3$ model star, the cross sections were modified one by one assuming uncertainties of 30% for the stable and 50% for the unstable isotopes involved. For each of these modifications, the *s*-process production factors are listed in Table VII; all normalized to the standard case.

The abundances of ^{206}Pb and ^{207}Pb exhibit the typical *s*-process behavior, i.e., they are scaling with the inverse of their (n,γ) cross sections. This means that these abundances are, at most, weakly dependent on a particular *s*-process model. As noted in Ref. [24] these two isotopes are particularly suited for constraining the *r*-abundance predictions required for deriving the U/Th ages of metal poor halo stars. In contrast, the ^{208}Pb abundance shows almost no response to the assumption of a smaller cross section. However, the reduction affects the ^{209}Bi abundance because more of the reaction flow is trapped already by ^{208}Pb. In any case, the very

TABLE VII. Sensitivity of the *s*-process production factors of the Tl-Pb-Bi isotopes with respect to variations of the relevant stellar cross sections.

Isotope with cross section factor	*s* production factors[a]						
	^{203}Tl	^{205}Tl	^{204}Pb	^{206}Pb	^{207}Pb	^{208}Pb	^{209}Bi
^{203}Tl×0.7	1.38	0.97	0.96	0.99	0.99	1.00	1.00
^{204}Tl×0.5	1.00	1.00	1.12	1.01	0.99	1.00	1.00
^{205}Tl×0.7	1.00	1.27	1.00	1.03	1.00	0.99	0.99
^{204}Pb×0.7	1.00	0.93	1.25	0.98	1.00	1.00	1.00
^{205}Pb×0.5	1.00	1.40	1.00	0.95	0.99	1.00	1.00
^{206}Pb×0.7	1.00	1.00	1.00	1.33	0.99	0.98	0.97
^{207}Pb×0.7	1.00	1.00	1.00	0.99	1.42	0.97	0.96
^{208}Pb×0.7	1.00	1.00	1.00	0.95	0.97	1.02	0.71
^{209}Bi×0.7	1.00	1.00	1.00	0.97	0.99	1.00	1.17

[a]Relative to the standard case for $M=3M_{\odot}$, [Fe/H]=−1.3.

small (n,γ) cross sections of ^{208}Pb and of ^{209}Bi imply an almost complete absorption of the reaction flow. Hence, additional contributions to the ^{206}Pb and ^{207}Pb abundances due to recycling from the region of α-unstable nuclei beyond $A=209$ are negligible. Also the cross sections of the unstable branch point isotopes ^{204}Tl and ^{205}Pb have little impact on the abundances of the stable Pb isotopes.

According to the status summarized in Table VI, the sensitivity study shows that the actual present cross section uncertainties give rise to uncertainties of about 7%, 6%, 19%, and 6% in the *s* abundances of ^{204}Pb, ^{206}Pb, ^{207}Pb, and ^{208}Pb, respectively. Apart from ^{207}Pb, the quality of the cross sections are almost satisfying the request that the *s* abundances should be affected by less than 5% uncertainty contributions due to the nuclear physics input. The good agreement of the present activation measurement on ^{208}Pb with the results of the corresponding TOF measurement indicates that systematic uncertainties seemed to be realistically evaluated in the latter case. Nevertheless, further improvements are certainly important if the Pb abundances are to be used to constrain astrophysical models via the $A=204/205$ branchings or the termination effect of the neutron magic isotopes with $N=126$.

This is certainly also true for refined analyses of the U/Th clock discussed in Ref. [24]. Since the *s* abundances of ^{206}Pb and ^{207}Pb are robust with respect to uncertainties in the *s*-process models, their *r* components are defined by subtraction from the solar values, $N_r=N_{\odot}-N_s$. These *r* abundances consist of two fractions, the radiogenic part due to the U/Th decay and the part from the decay of the primary *r*-process yields at $A=206$ and 207. According to the abundance tables of Arlandini *et al.* [26], the *s* process accounts for 58% and 64% of the solar ^{206}Pb and ^{207}Pb abundances, respectively. The *s* abundances in Ref. [26] were adopted from an AGB model of half solar metallicity, which was shown to best reproduce the main component in the solar system. To reproduce the strong component, one must consider that the major *s* contribution to solar ^{208}Pb actually derives for AGB stars of about 1/10 solar metallicity [27]. According to the Galactic Chemical Evolution (GCE) study of Travaglio *et al.* [5] the contributions from all previous generations of AGB stars to the ^{204}Pb and ^{206}Pb abundances at the epoch of solar system formation are 96% and 63%, quite close to the Arlandini *et al.* predictions of 94% and 58%, whereas the corresponding values for ^{204}Pb, ^{208}Pb, and ^{209}Bi are significantly larger (82%, 95%, and 19% instead of 64%, 34%, and 5%, respectively).

Neglecting all uncertainties but those of the present cross section data, one obtains 37±6% and 18±18% for the *r* components of ^{206}Pb and ^{207}Pb with respect to solar. With better cross section data, these values could be determined with improved uncertainties of less than 10%. This step would be instrumental for a stringent test of the *r*-process calculations required in evaluating the U/Th ages of metal-poor halo stars.

In this context the radiogenic Pb/Bi abundance ratios in these stars could possibly be used as an independent test, provided (i) that the abundance uncertainties originating from the cross section data must be significantly smaller than the contributions from the primary *r*-process yields, (ii) that model predictions for the dominant *s* abundance of ^{208}Pb are well under control, and (iii) that the accuracy of the lead abundances in halo stars can be improved to match the quality of the U/Th data. The first point clearly calls for improved cross section data, in particular, for ^{207}Pb.

IV. SUMMARY AND OUTLOOK

The activation technique has been used to measure the very small (n,γ) cross section of ^{208}Pb as well as the dominant partial (n,γ) cross section of ^{209}Bi leading to the ground state of ^{210}Bi at astrophysically relevant energies with uncertainties around 6%. In both cases, the activation technique provides firm information on the direct capture component, which contributes a major part of these cross sections, but cannot be detected in time-of-flight experiments.

These results together with previously reported cross sections [20] were used to investigate the *s*-process abundances in the Tl/Pb/Bi region for the asymptotic giant branch phase of a $3M_{\odot}$ and [Fe/H]=−1.3 model star. The aim of this study was to analyze the branchings at $A=204/205$, the re-

cycling effect from the α-unstable region beyond ^{209}Bi, and to constrain the *r*-process components of the isotopic Pb abundances. This was carried out by means of a detailed reaction network at the *s*-process end point, including the complex competition between neutron captures and a number of β and α decays. As an important aspect, the sensitivity of the calculated *s* abundances on the uncertainties of the stellar (n,γ) rates was also considered in this study.

It was found that α recycling from the trans-bismuth region is almost negligible because the reaction flow is mostly trapped by the very small ^{208}Pb cross section. An unbiased decomposition of the *s* and *r* components can be achieved for ^{206}Pb and ^{207}Pb, whereas the other Pb isotopes may be affected by the underlying stellar *s*-process model and must, therefore, be treated in a more comprehensive way. Nevertheless, the present findings indicate that the *r* components of the Pb isotopes can be determined with the required accuracy for constraining the calculated *r*-process abundance distributions in analyses of the U/Th ages of very metal-poor halo stars.

While preliminary arguments can already be based on the existing cross section information, a detailed quantitative discussion requires more accurate data. Hence, further efforts should be directed to improved cross section measurements aiming at uncertainties of $<5\%$.

ACKNOWLEDGMENTS

We thank D. Roller and E.-P. Knaetsch for their support during the measurements, G. Rupp and H. Müller for their excellent technical assistance, as well as P. Galati for preparing part of the figures. This work was supported by the Joint Institute for Nuclear Astrophysics (JINA) through NSF Grant No. PHY-0140324, and partly by the Italian MIUR-FIRB grant "The astrophysical origin of the heavy elements beyond Fe."

[1] P. Seeger, W. Fowler, and D. Clayton, Astrophys. J. **97**, 121 (1965).
[2] D. Clayton and M. Rassbach, Astrophys. J. **148**, 69 (1967).
[3] F. Käppeler, H. Beer, and K. Wisshak, Rep. Prog. Phys. **52**, 945 (1989).
[4] C. Travaglio, D. Galli, R. Gallino, M. Busso, F. Ferrini, and O. Straniero, Astrophys. J. **521**, 691 (1999).
[5] C. Travaglio, R. Gallino, M. Busso, and R. Gratton, Astrophys. J. **549**, 346 (2001).
[6] R. Cayrel *et al.*, Nature (London) **409**, 691 (2001).
[7] C. Sneden, Nature (London) **409**, 673 (2001).
[8] B. Pagel, in *Astrophysical Ages and Dating Methods*, edited by E. Vangioni-Flam, M. Cassé, J. Audouze, and J. Tran Thanh Van (Editions Frontières, Gif-sur-Yvette, 1990), p. 493.
[9] K. Takahashi and K. Yokoi, At. Data Nucl. Data Tables **36**, 375 (1987).
[10] P. Mutti, F. Corvi, K. Athanassopoulos, H. Beer, and P. Krupchitsky, in *Nuclei in the Cosmos V*, edited by N. Prantzos and S. Harissopoulos (Editions Frontières, Paris, 1998), p. 204.
[11] H. Beer, F. Corvi, and P. Mutti, Astrophys. J. **474**, 843 (1997).
[12] H. Beer, W. Rochow, F. Käppeler, and T. Rauscher, in *Nuclei in the Cosmos VII*, edited by S. Kubono, T. Teranishi, T. Kajino, K. Nomoto, and I. Tanihata; Nucl. Phys. **A718**, 518c (2003).
[13] H. Beer and F. Käppeler, Phys. Rev. C **21**, 534 (1980).
[14] W. Ratynski and F. Käppeler, Phys. Rev. C **37**, 595 (1988).
[15] M. Igashira, in *Book of Presentations, Japan-Russia LBE Coolant Workshop*, edited by H. Sekimoto, T. Obara, and G. Toshinsky, Bulletin of the Research Laboratory for Nuclear Reactors, Special Issue No. 4, p. 135 (Tokyo Institute of Technology, Tokyo, 2001); (private communication).
[16] S. Jaag and F. Käppeler, in *Nuclei in the Cosmos '90*, edited by H. Oberhummer and W. Hillebrandt (Max-Planck-Institut für Physik und Astrophysik, Garching, 1990), Report MPA/P4, p. 250.
[17] S. F. Mughabghab, *Neutron Cross Sections* (Academic Press, Orlando, 1984), Vol. I, Part B.
[18] A. Letourneau *et al.*, in *Capture Gamma-Ray Spectroscopy and Related Topics*, edited by J. Kvasil, P. Cejnar, and M. Krtička (World Scientific, New Jersey, 2003), p. 734.
[19] S. F. Mughabghab, M. Divadeenam, and N. E. Holden, Neutron Cross Sections (Academic Press, New York, 1981), Vol. I, Part A.
[20] Z. Y. Bao, H. Beer, F. Käppeler, F. Voss, K. Wisshak, and T. Rauscher, At. Data Nucl. Data Tables **76**, 70 (2000).
[21] M. Mizumoto, S. Raman, R. L. Macklin, G. G. Slaughter, J. A. Harvey, and J. H. Hamilton, Phys. Rev. C **19**, 335 (1979).
[22] A. R. de L. Musgrove and R. L. Macklin, Australian Atomic Energy Commission Technical Report No. AAEC/PR46, 1979, p. 16.
[23] R. Gallino, C. Arlandini, M. Busso, M. Lugaro, C. Travaglio, O. Straniero, A. Chieffi, and M. Limongi, Astrophys. J. **497**, 388 (1998).
[24] J. Cowan, B. Pfeiffer, K.-L. Kratz, F.-K. Thielemann, C. Sneden, S. Burles, D. Tytler, and T. C. Beers, Astrophys. J. **521**, 194 (1999).
[25] W. Aoki, S. G. Ryan, J. E. Norris, T. C. Beers, H. Ando, and S. Tsangarides, Astrophys. J. **580**, 1149 (2002).
[26] C. Arlandini, F. Käppeler, K. Wisshak, R. Gallino, M. Lugaro, M. Busso, and O. Straniero, Astrophys. J. **525**, 886 (1999).
[27] M. Busso, R. Gallino, and G. J. Wasserburg, Annu. Rev. Astron. Astrophys. **37**, 239 (1999).